

Article

Orange-Peel-Derived Carbon: Designing Sustainable and High-Performance Supercapacitor Electrodes

C. K. Ranaweera¹, P. K. Kahol², M. Ghimire³, S. R. Mishra³ and Ram K. Gupta^{1,*}

¹ Department of Chemistry, Pittsburg State University, Pittsburg, KS 66762, USA; cranaweera@gus.pittstate.edu

² Department of Physics, Pittsburg State University, Pittsburg, KS 66762, USA; pkahol@pittstate.edu

³ Department of Physics, The University of Memphis, Memphis, TN 38152, USA; mghimire@memphis.edu (M.G.); srmishra@memphis.edu (S.R.M.)

* Correspondence: rgupta@pittstate.edu; Tel.: +1-620-235-4763

Received: 27 July 2017; Accepted: 7 August 2017; Published: 8 August 2017

Abstract: Interconnected hollow-structured carbon was successfully prepared from a readily available bio-waste precursor (orange peel) by pyrolysis and chemical activation (using KOH), and demonstrated its potential as a high-performing electrode material for energy storage. The surface area and pore size of carbon were controlled by varying the precursor carbon to KOH mass ratio. The specific surface area significantly increased with the increasing amount of KOH, reaching a specific surface area of 2521 m²/g for a 1:3 mass ratio of precursor carbon/KOH. However, a 1:1 mass ratio of precursor carbon/KOH displayed the optimum charge storage capacitance of 407 F/g, owing to the ideal combination of micro- and mesopores and a higher degree of graphitization. The capacitive performance varied with the electrolyte employed. The orange-peel-derived electrode in KOH electrolyte displayed the maximum capacitance and optimum rate capability. The orange-peel-derived electrode maintained above 100% capacitance retention during 5000 cyclic tests and identical charge storage over different bending status. The fabricated supercapacitor device delivered high energy density (100.4 μWh/cm²) and power density (6.87 mW/cm²), along with improved performance at elevated temperatures. Our study demonstrates that bio-waste can be easily converted into a high-performance and efficient energy storage device by employing a carefully architected electrode—electrolyte system.

Keywords: activated carbon; bio-waste; energy storage; orange peel; supercapacitor

1. Introduction

Supercapacitors or electrical double-layer capacitors (EDLCs) are one of the advanced energy storage devices that have been drawing significant attention lately because of their unique advantages such as pulse power supply, rapid charging time, outstanding service life, and operational safety [1,2]. Supercapacitors are emerging as a substitute power source over conventional batteries for a wide range of applications in electrical vehicles, portable electronics, and energy harvesting systems [3,4]. Accumulation of charges on the electrode/electrolyte interface leads to electrical energy storage in EDLCs. Therefore, an electrode with a larger surface area is necessary to maximize the charge storage capacity. So far, various forms of carbons including grapheme [5], carbon nanotubes (CNT) [6], carbon nanofibers [7], and carbon nanospheres [8] have been exploited for supercapacitor applications due to their exceptional electrochemical and physical properties. Tedious synthesis processes and the relatively high cost of these carbon allotropes limit their extensive use in commercial energy storage devices. In contrast, activated carbon represents a cost-effective and facile synthesis process for carbon-based electrodes compared to more advanced carbon allotropes. Activated carbon with a

highly porous structure offers a larger surface area for electrolyte ion adsorption and electrostatic double layer formation, which enhances the capacity.

Currently, the scarcity of petrochemical feedstock and environmental issues have driven the focus towards sustainable and renewable resources for energy generation and storage. Therefore, converting bio-waste into useful carbon material is gathering more and more attention. Bamboo [9], corncob residue [10], sugarcane bagasse [11], waste tea leaves [12], rice bran [13], plant leaves [14], and banana peel [15] have been utilized as precursors to prepare activated carbon for electrodes in supercapacitors. Preparation of activated carbons involves two processes: pyrolysis of the precursor in an inert environment, accompanied by chemical or physical activation at a higher temperature. Steam [16] and carbon dioxide [17] are the main physical activators. Chemical activation agents such as KOH [18], NaOH [19], H₃PO₄ [20], and ZnCl₂ [21] have been employed to introduce porosity to carbon for numerous applications. Among them, KOH is the most attractive chemical reagent for the activation process of carbon used in supercapacitors, because it produces high carbon yield, high porosity, precise pore size distribution, and ultrahigh surface area (~1 mL/g and ~3000 m²/g) [22,23]. Apart from the surface area and pore characteristics, the charge storage capacity of a supercapacitor depends on the surface functionality. Incorporation of a surface functional group containing oxygen [24], nitrogen [25], and sulfur [26] can induce pseudocapacitive behavior and increase wettability to improve the capacitance.

According to the latest statistics from the United States Department of Agriculture (USDA), estimated global orange production reached 49.6 million metric tons in 2016–2017 [27]. Among those, a significant percentage of oranges are processed to manufacture fruit juice, 50–60% of which is discarded as waste [28,29]. A major portion of the waste consists of orange peel, which accounts for about 44% of the total weight of the orange fruit [30]. As a widely available and readily collectable industrial bio-waste, various applications including extraction of pectin [31], heavy metal adsorption [32], dye adsorption [33], production of biofuel [34], and starting material for polymers [35] have been proposed for orange peel to date. Supercapacitors in general consist of two electrodes, which are coated with porous materials such as activated carbon. This creates a higher surface area for efficient charge storage. A carbon-based commercial supercapacitor cell delivers a specific capacitance of 25–30 F/g. Power density and energy density are two important parameters that can be used to evaluate the performance of an energy storage device. The power density of a commercial supercapacitor is 3–5 kW/kg, which is higher than 1 kW/kg for a similar size battery. The main limitation of a supercapacitor is the lower energy density (~10 Wh/kg). In contrast, batteries deliver an energy density of 35–40 Wh/kg. The cycle life of a supercapacitor is around 500,000 cycles.

Petrochemical coke is a widely used source of activated carbon. In this study, we introduce an attractive alternative, waste orange peel, to produce activated carbon. It is a low-cost, widely available, and sustainable source of carbon. An orange-peel-based supercapacitor demonstrated high performance by reaching a capacitance above 400 F/g, energy density of 100.4 μWh/cm², and power density of 6.87 mW/cm². Although this study evaluated the use of activated carbon for supercapacitors, there have been numerous reports on the application of activated carbon as an electrode material in batteries. Herein, we report the synthesis and method to control the surface area and pore characteristics of carbon derived from orange peel. A combination of KOH and precursor (1:1 *w/w*) produced carbon with a moderate specific surface area, a high degree of graphitization, and, most importantly, a well-developed meso-/micropore structure, which exhibited an optimum charge storage capacity of 407 F/g at a current density of 0.5 A/g. The effect of different alkali electrolytes on electrochemical performance was studied in detail and it is noted that KOH electrolytes offer excellent rate capability and capacitance. About 100% capacitance retention over 5000 charge–discharge cycles, unchanged electrochemical performance in various bending status, and improved capacitance at elevated temperatures demonstrate the potential applicability of activated carbon from orange peel in high-performance electrodes for energy storage applications.

2. Results and Discussion

Waste orange peels were converted to porous carbon through pre-carbonization and pyrolysis in the presence of a chemical activator, as illustrated in the graphical abstract. Subsequently, synthesized carbon was utilized to fabricate an electrode for symmetric supercapacitor. Figure 1a displays the XRD patterns of unactivated and activated carbonized OP with different mass ratios of KOH. XRD peaks centered around 2θ of 24° and 44° in all the activated carbon samples correspond to the (002) and (100) planes of the graphitic carbon. Broad and low-intensity peaks indicate the disordered nature of the carbon samples. The characteristics peaks become broader and reduce intensity with KOH mass ratio increase from 0 to 3, suggesting the decrease in graphitic structure in the OPACs [5]. These observations revealed that the degree of graphitization of the carbon sample was governed by a chemical activation agent. Further, the graphitic structure of unactivated and activated carbons was investigated by Raman spectra (Figure 1b). Two characteristic peaks around 1340 and 1582 cm^{-1} were assigned for the D-band and G-band of carbon, respectively. The D-band corresponds to the sp^3 hybridized disordered carbon phase, while the G-band relates to the sp^2 hybridized graphitic phase of the carbon [36,37]. The proportion of the disordered carbon presence in a sample can be described by the relative intensity of the D-band and G-band (the I_D/I_G ratio). The I_D/I_G ratio for OPUAC was 0.88, whereas the I_D/I_G ratios for OPAC-0.5, OPAC-1, OPAC-2, and OPAC-3 were found to be 0.91, 0.90, 0.91, and 0.96, respectively—considerably higher than in the unactivated carbon sample. The rise of the I_D/I_G ratio for the KOH-activated carbon suggests that harsh chemical treatment disturbed the structural order of the carbon. However, the graphitization level of our activated carbon materials ($I_G/I_D > 1.04$) were significantly higher than the I_G/I_D ratio of commercially activated carbon (0.52) [11], indicating its suitability as an electrode material due to the excellent electrical conductivity. The high electrical conductivity of carbon derived from orange peel will reduce the charge-transfer resistance for the electrolyte ions and thus improve the electrochemical properties.

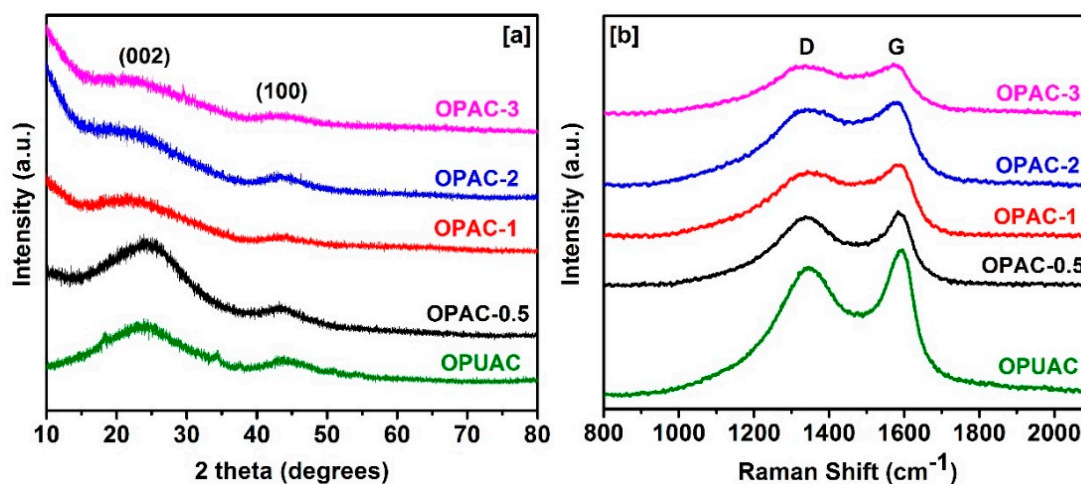


Figure 1. (a) XRD spectra and (b) Raman spectra of OPUAC and OPACs carbons.

We analyzed the pyrolysis behavior of orange peel precursor under a nitrogen atmosphere using thermogravimetric analysis. Thermogravimetric (TG) and its derivative (DTG) curves are given in Figure S1. Generally, the pyrolysis of biomass involves the thermal decomposition of lignocellulosic biomass by releasing volatile matter and leaving char behind. As seen in the DTG curve, the appearance of peaks at temperature ranges of $50\text{--}100^\circ\text{C}$, $200\text{--}300^\circ\text{C}$, and $300\text{--}400^\circ\text{C}$ can be attributed to the dehydration of orange peel, the decomposition of hemicellulose, and the decomposition of cellulose, respectively [38,39]. Lignin pyrolyzes steadily over a wide temperature range, and the weaker peak between 430 and 500°C may represent the decomposition of lignin. Lignin contributes predominantly to the formation of char [40,41]; about 21% char yield was observed

at 700 °C. The SEM images in Figure 2 revealed the effect of chemical activation and pyrolysis on the morphology of carbon synthesized from the orange peel precursor. The pyrolysis of the pre-carbonized precursor in the presence of KOH (the chemical activating agent) produced open channels with non-uniform honeycomb-like morphologies on the surface (Figure 2a–d). The pyrolysis of the pre-carbonized precursor without employing a chemical activating agent produced a sheet-like structure (Figure 2e). More prominent and widely spread honeycomb-like structures were observed with an increasing KOH mass ratio. The schematic of the honeycomb and open tubular channels' structures is illustrated in Figure 2f. The presence of an open channel structure forms porous carbon, which provides electrolyte ions a higher surface area to access and a path for transportation during the charge storage process [42,43]. The activation of the carbon by KOH at 800 °C proceeded according to the following reaction:



Subsequently, K_2CO_3 decomposed and the resultant products further reacted with the carbon to form hollow channels inside the carbon matrix [44,45].

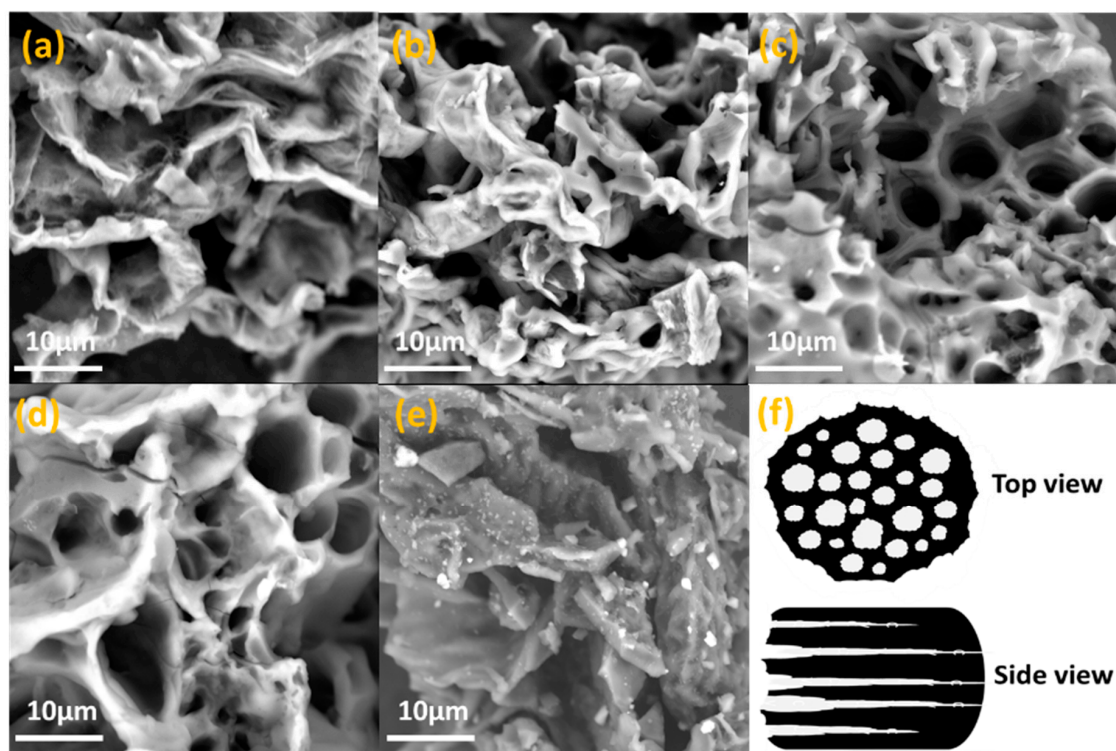


Figure 2. SEM image of (a) OPAC-0.5; (b) OPAC-1; (c) OPAC-2; (d) OPAC-3; (e) OPUAC; and (f) a schematic diagram of the porous structure in carbon derived from OP.

The nitrogen adsorption–desorption isotherms of OPAC and OPUAC samples are illustrated in Figure 3a. It is evident that the pore structure and specific surface area of the resultant carbon are influenced by the mass ratio of the activating agent. OPAC-2 and OPAC-3 showed type I isotherm curves with the majority of N_2 adsorption at relative pressures (P/P_0) below 0.3 and a near-parallel slope (to x-axis) of the isotherm above 0.3 of P/P_0 , which is typical of micropores in carbon. On the other hand, OPAC-0.5 and OPAC-1 showed a combination of type I and IV isotherm curves with a sharp slope at relative pressure less than 0.1, followed by a steady increase in the N_2 adsorption and the appearance of distinguishable hysteresis loops at P/P_0 over 0.5, demonstrating the existence of both micropores and mesopores [46]. In contrast, very low N_2 adsorption of OPUAC indicated the almost non-existence of the porous structure.

These observations were further confirmed by the BJH pore size distribution plot (Figure 3b). The pore size of OPAC-1 and OPAC-0.5 was mainly in the 3–4 nm range, along with a smaller fraction of pores around 2 nm, whereas OPAC-2 and OPAC-3 did not exhibit a complete distribution at the smaller pore size end and overwhelmingly consisted of pores with a diameter of less than 2 nm. Therefore, the structure of OPAC-1 and OPAC-0.5 was a combination of meso- and micropores with a larger proportion of mesopores. OPAC-2 and OPAC-3 contained an abundance of micropores. Table 1 summarizes the pore characteristics of the carbon materials. The specific surface area of the OPAC-0.5 to OPAC-3 continuously increased from 1004 to 2521 m²/g; similarly, pore volume also increased from 0.52 to 1.30 cm³/g. We observed significantly lower specific surface area and pore volume for OPUAC (0.852 m²/g and 0.0004 cm³/g, respectively). Nevertheless, pore diameter was reduced in the activated OP samples from 1.69 to 1.04 nm as the KOH mass ratio increased from 0.5 to 3. It was obvious that the progressive increase of the KOH mass ratio during the activation process continued to etch the carbon matrix deeper, while maximizing the pore volume and surface area, instead of enlarging pore diameter. Therefore, a substantial proportion of micropores were created at higher KOH mass ratios.

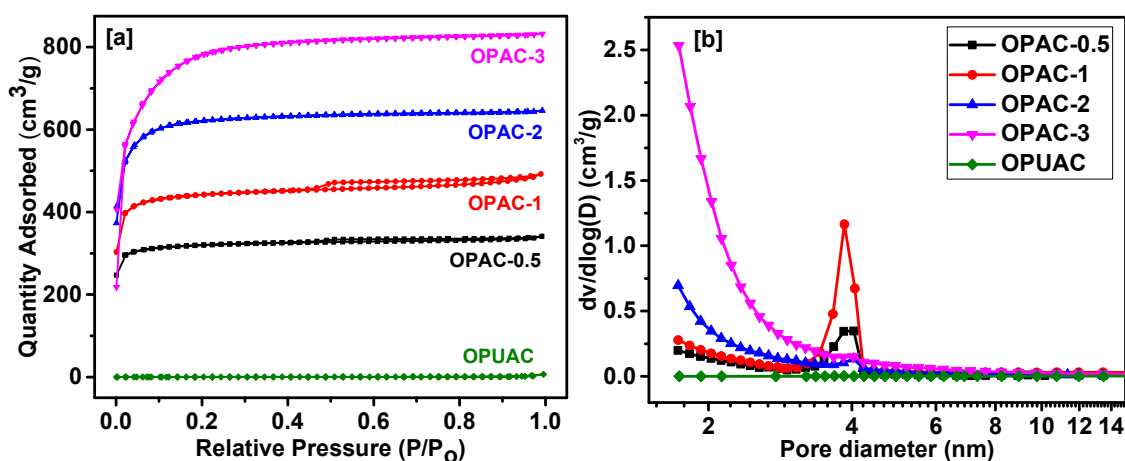


Figure 3. (a) Nitrogen adsorption–desorption isotherms and (b) BJH pore size distributions of OPUAC and OPAC carbons.

Table 1. Pore characteristics and surface area of unactivated and activated carbons. ^a Surface area measured via BET method, ^b Total pore volume, and ^c Average pore diameter.

Sample	S _{BET} ^a (m ² /g)	V _{total} ^b (cm ³ /g)	D _{ave} ^c (nm)
OPAC-0.5	1004	0.52	1.69
OPAC-1	1391	0.72	1.59
OPAC-2	1960	1.01	1.45
OPAC-3	2521	1.30	1.04
OPUAC	0.852	0.0004	1.16

The existence of both micro- and mesopores is a favorable feature in activated carbon-based electrodes for supercapacitor applications. The presence of micropores provides a larger surface for the adsorption–desorption process of electrolyte ions. Mesopores also ensure a highly accessible surface area and offer wider channels for several electrolyte ions to diffuse at the same time without experiencing geometric resistance [14,47]. Therefore, we presumed superior electrochemical performance in OPAC-1 due to the higher fraction of mesopores and enhanced surface area.

The electrochemical performance of supercapacitor electrodes based on orange-peel-derived carbon was studied by employing a three-electrode system in 3 M KOH electrolyte. Figure 4a compares the cyclic voltammetry curves of OPUAC and OPACs at a scan rate of 10 mV/s. OPAC

electrodes exhibited symmetrical rectangular-shaped CV curves. In the absence of any redox peaks, this represents a typical electric double-layer (EDL) mechanism. In contrast, OPUAC had a smaller and highly distorted rectangular CV curve, indicating low charge storage capacity compared to OPAC electrodes. Galvanostatic charge–discharge profiles at a current density of 1 A/g and specific capacitance at different current densities for the OPUAC and OPACs electrodes are shown in Figure 4b. The symmetric and linear nature of the charge–discharge profiles provided further evidence of the EDL behavior of the electrodes. The shortest discharging time and lowest capacitance of 115 F/g at 1 A/g were given by OPUAC. Chemical activation of the pre-carbonized OP significantly enhanced the capacitance. OPAC-1 provided the highest capacity of 217 F/g at 1 A/g (Figure 4c). OPAC-2 and OPAC-3 had a higher specific surface area than OPAC-1, indicating that increased chemical activator amount and high surface area did not always improve the charge storage capacity. Higher specific surface area of the OPAC-2 and OPAC-3 was attained through the substantial presence of micropores. However, very narrow micropores restrict the ion transfer process, reducing the effective surface area for electrolyte ion adsorption. Therefore, the OPAC-1 electrode provided the maximum capacitance.

Electrochemical properties of the OPAC-1 electrode were studied in detail by performing CV at different scan rates (Figure 4d) and GCD at different current densities (Figure S2). At low scan rates, CV curves exhibited a nearly perfect rectangular shape and the shape was retained even at higher scan rates with a minor distortion, suggesting a rapid and unrestricted charge transfer process, owing to the meso-/micropore combination of OPAC-1. As seen in Figure S2, the charge–discharge profiles retained their linear and almost symmetrical nature even at higher current densities, indicating an efficient electrolyte ion diffusion process. The IR drop (voltage drop) at the start of the discharge curve accounts for the total resistance in the electrode [48]. We observed an IR drop of 4 mV at 0.5 A/g and it only increased to 194 mV even for a high discharge current of 20 A/g (Figure S3).

Figure 4e illustrates the CV curves for different bending angles at a scan rate of 100 mV/s. The shape of the CV curves remained identical, indicating that the OPAC-1 electrode sustained its electrochemical properties while flexing. This suggested a potential application of OPAC-1 electrode in flexible supercapacitors. The long-term cyclic stability of a supercapacitor is another important feature that determines its practical applicability. The cyclic stability of OPAC-1 was evaluated by performing continuous charge–discharge cycles at 3A/g (Figure 4f). The capacitance for the first 500 cycles gradually increased until capacitance retention reached 105%, followed by an almost steady capacitance delivery. The capacitive performance improved to 108% of its initial value over 5000 cycles. The initial improvement in capacitance was due to the activation of the OPAC-1 electrode by progressive wetting of the electrode with electrolytes [10,49]. The perfectly overlapping charge–discharge profiles of the first and last five cycles (inset in Figure 4f) provided further evidence for the excellent long-term cyclic stability of OPAC-1.

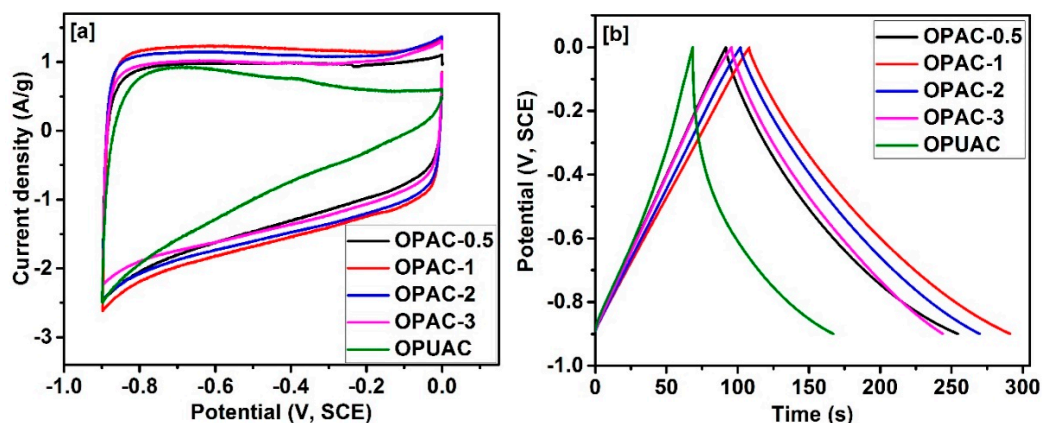


Figure 4. Cont.

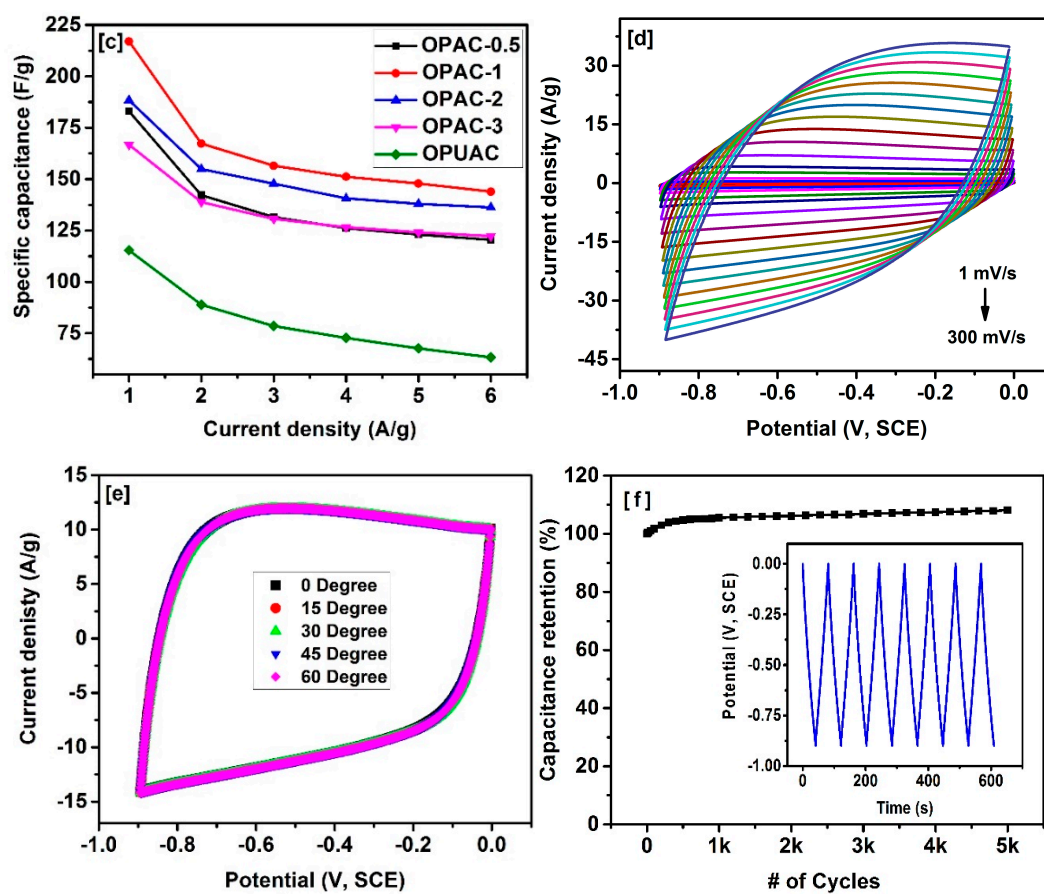


Figure 4. (a) CV curves at the scan rate of 10 mV/s; (b) GCD profiles at the current density of 1 A/g; (c) specific capacitances at different current densities; (d) CV curves of OPAC-1 at various scan rates. (e) CV curves of OPAC-1 for various bending angles at the scan rate of 100 mV/s; and (f) cyclic stability of OPAC-1 at current density of 2 A/g for 5000 cycles; inset shows GCD profiles of the first and last few cycles.

To understand the effect of electrolytes, specific capacitance of OPAC-1 was measured in 3 M KOH, NaOH, and LiOH at different current densities (Figure 5a) and scan rates (Figure 5b). According to the results, OPAC-1 in KOH electrolyte delivered superior specific capacitance than NaOH and LiOH electrolytes. The improved electrochemical properties in KOH can be ascribed to the smaller hydrated ionic radius of K^+ (3.31 Å), which is lower than the hydrated ionic radius of the Na^+ (3.58 Å) and Li^+ (3.82 Å). The ionic conductivity of hydrated ions increases with a decrease in ion size [47]. This facilitated access to the innermost pores of OPAC-1 for the K^+ and reduced the transition time between the adsorption and desorption processes. Therefore, OPAC-1 in KOH electrolyte exhibited the maximum charge storage capacity. We also observed a different rate behavior of OPAC-1 in these electrolytes. Figure S4 displays the CV curves of OPAC-1 at 10 and 200 mV/s in KOH, NaOH, and LiOH. The areas under the curves were almost equal at a low scan rate, indicating similar charge storage behavior in the three electrolytes. In contrast, charge storage capacity deviated at a high scan rate, increasing in the order of LiOH < NaOH < KOH. The least decay of capacitance in KOH electrolyte can be credited to the smallest hydrated radius of K^+ among the three metallic ions. Therefore, hydrated K^+ possessed the highest ionic conductivity and shortest relaxation time during the diffusion process, resulting in an increment in the rate capability of OPAC-1 in LiOH < NaOH < KOH, in this order.

Additionally, electrochemical impedance spectra were conducted to understand the electrochemical behavior of OPAC-1 in three different electrolytes. Figure 5c shows the Nyquist plots of the OPAC-1 electrode in 3 M KOH, NaOH, and LiOH in a frequency range from 10 kHz to 0.05 Hz. Nyquist plots of

the three electrolytes had a similar shape: a modest semi-circle at the middle to high frequency range, and a straight line at low frequency. Interception at Zreal axis at a high frequency (inset Figure 5c) was an indication of the solution resistance [50]. The corresponding values for the solution resistance (R_S) were 0.83, 0.58, and 0.36 Ω for LiOH, NaOH, and KOH, respectively. Therefore, the KOH electrolyte had better conductivity than NaOH and LiOH electrolytes. The diameter of the semicircle represented the charge transfer resistance at the double layer [51], which was decreasing in the following sequence, LiOH > NaOH > KOH. The lowest charge transfer resistance value in KOH electrolyte suggests that K^+ contributed to an efficient charge adsorption–desorption process on the electrode–electrolyte interface due to its smaller hydrated ionic radius [52]. At the low frequency range, we observed a near-vertical straight line for KOH electrolyte, indicating perfect capacitive behavior and efficient ionic diffusion. We simulated the equivalent circuit for the EIS data to obtain the quantitative value for each electrochemical component of the electrode. The equivalent circuit and parameters of the OPAC-1 in the three electrolytes are given in Figure 5d. Equivalent circuit included the components related to solution resistance (R_S), charge transfer resistance (R_{CT}), constant phase elements (Q_1 and Q_2), and capacitance (C). Existence of the constant phase elements in the electrode can be attributed to the capacitance of the double layer, the chaotic nature of the diffusion process, or irregularities in the electrode–electrolyte interface [53]. According to the simulated values, total capacitance in three electrolytes increased in the order of LiOH < NaOH < KOH, which was consistent with the charge storage capacitance calculated from GCD and CV measurements (Figure 5a,b). Bode plots (frequency vs. impedance) of three different electrolytes further confirmed the outstanding rate capability in KOH electrolyte (Figure S5). At a low frequency range (<1 Hz), differences between the impedances in three electrolytes were insignificant. Beyond a frequency of 1 Hz, a low impedance was observed for KOH compared to NaOH and LiOH, indicating an excellent rate capability in KOH electrolyte.

OPAC-1 produced the optimum specific capacitance of 407 F/g at 0.5 A/g in 3 M KOH electrolyte. However, we noticed a decrease in specific capacitance with increasing current density. This is an effect of limited electrolyte ions' diffusion to the micropores and decreased the amount of electrolyte ions that accumulated on the electrode surface, owing to insufficient time at higher current densities [51,54]. Here, we report the specific capacitance for OPAC-1 electrode, superior or comparable to the capacitance of previous biomass-derived electrodes. Table 2 displays the capacitive performance of the recently synthesized activated carbon from the biomass precursors. It should be noted that the charge storage capacity of OPAC-1 was higher than commercially available activated carbons (<200 F/g) [55], and even comparable to the more advanced forms of carbons such as graphene-based materials (100–347 F/g) [56], nitrogen-doped graphene (138–326 F/g) [57], and CNT (128–335 F/g) [58]. The high capacitive performance of our material can be attributed to the higher specific surface area along with the prominent mesopore structure, with a 3–4 nm pore size. This provided a larger surface area for the adsorption–desorption process of the ions and efficient pathways to ion transfer.

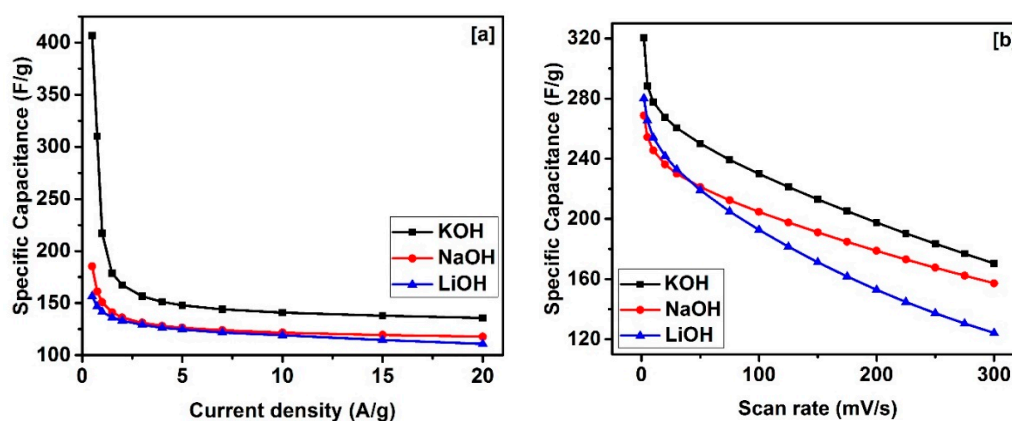


Figure 5. Cont.

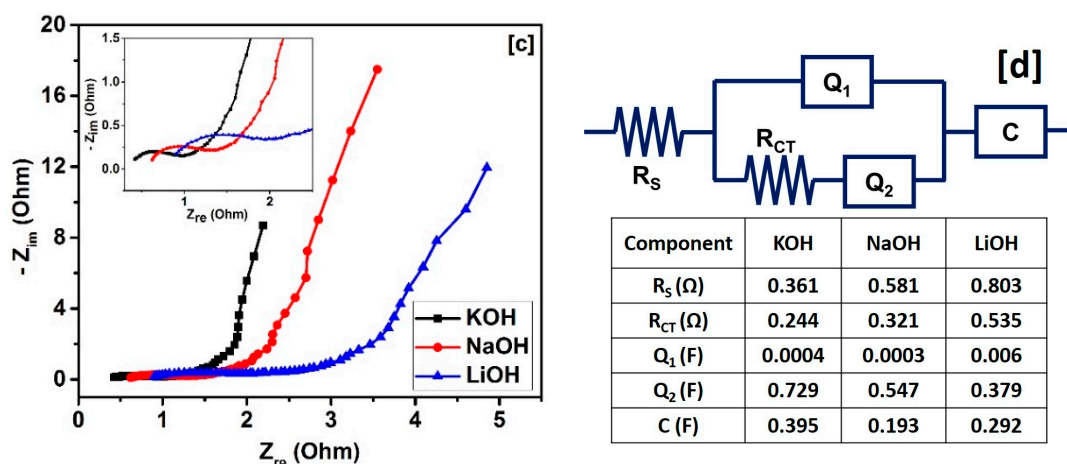


Figure 5. (a) Specific capacitances at different current densities; (b) specific capacitances at various scan rates; (c) Nyquist plots with inset displaying magnification at higher frequency region; and (d) equivalent circuit obtained from simulating the EIS data and fitting values for the components of the equivalent circuit for OPAC-1 electrode.

Table 2. Comparison of the orange-peel-derived carbon to carbon derived from other biomass precursors.

Carbon Source	BET Surface Area (m^2/g)	Specific Capacitance (F/g)	Current Density (A/g)	Electrolyte	Reference
Pitch	2602	263	0.05	6 M KOH	[59]
Porous starch	3251	304	0.05	6 M KOH	[60]
Celtuce leaves	3404	421	0.5	2 M KOH	[61]
Sago bark	58	113	0.02	5 M KOH	[62]
Corn straw	1413	379	0.05	6 M KOH	[63]
Bamboo	3061	258	0.1	6 M KOH	[64]
Oil palm kernel shell	462	210	0.5	1 M KOH	[48]
Rice husk	2696	147	0.1	6 M KOH	[65]
Ramie	1616	287	0.05	6 M KOH	[66]
Camellia oleifera shell	1935	266	0.2	6 M KOH	[67]
Soybean residue	1950	261	0.2	1 M H_2SO_4	[25]
Nem dead leaves	1230	400	0.5	1 M H_2SO_4	[14]
Orange peel	1391	407	0.5	3 M KOH	This work

Considering the high electrochemical performance of the OPAC-1, a symmetric supercapacitor was fabricated by assembling two OPAC-1 electrodes as the negative and positive electrodes. CV measurements were performed between 0 and 1 V in 3 M KOH electrolyte for various scan rates (Figure 6a). The OPAC-1-based supercapacitor exhibited a rectangular-shaped CV curve at low scan rates and continued to maintain a rectangular shape without major distortion with increasing scan rate, indicating its suitability as a fast charge–discharge supercapacitor device. The charge storage process of an energy storage device can be identified by the power law equation below:

$$i = av^b \quad (2)$$

where i is the peak current (A), v is the scan rate (V/s), and a and b are coefficients. The value of coefficient b determines whether the charge storage mechanism is either capacitive ($b = 1$) or semi-infinite diffusion controlled ($b = 0.5$) [68,69]. We plotted the logarithms of discharge current density vs. logarithms of scan rate (Figure S6) and obtained 0.89 for coefficient b . This suggests that the charge storage process of the OPAC-1 supercapacitor was based on the accumulation of electrical charges at the electrode–electrolyte interface.

GCD profiles for OPAC-1 supercapacitor at different current densities in Figure 6b resemble a quasi-triangle shape, further confirming the formation of EDL during the charge storage process. IR drop for the supercapacitor was negligible even for higher current densities, which provided evidence of the minimum internal resistance of the device. Figure 6c shows the specific capacitance of the OPAC-1-based supercapacitor at various current densities. The specific capacitance of the supercapacitor decreased from 729 to 697 mF/cm² as the current density increased from 2 to 14 mA/cm², demonstrating an impressive capacitance retention of 96% across the same current density range. This further confirmed the high rate capability of the OPAC-1 supercapacitor. The well-developed structure of OPAC-1 facilitated the high rate capability by providing an unhindered pathway to ion transfer.

The energy and power density of the OPAC-1 supercapacitor are illustrated using a Ragone plot in Figure 6d. The supercapacitor delivered energy density between 100.4 to 93.4 μWh/cm² for the corresponding power density from 0.99 to 6.87 mW/cm², while maintaining 93% of its highest energy density. We compared these values to previously reported supercapacitors based on other forms of carbon (inset Figure 6d). For example, the energy and power performance of polyaniline-deposited CNT (50.98 μWh/cm² at 28.404 mW/cm²) [70], a graphene oxide–polypyrrole composite (16.8 μWh/cm² at 0.08 mW/cm²) [71], a polypyrrole–MnO₂–CNT coated cotton thread (33 μWh/cm² at 0.67 mW/cm²) [72], CNT-coated carbon microfiber (9.8 μWh/cm² at 0.189 mW/cm²) [73], and graphene–cellulose paper (1.5 μWh/cm² at 0.01 mW/cm²) [74] were inferior to our work. The high power capability of the OPAC-1 supercapacitor indicates its potential for applications where rapid release of energy is required.

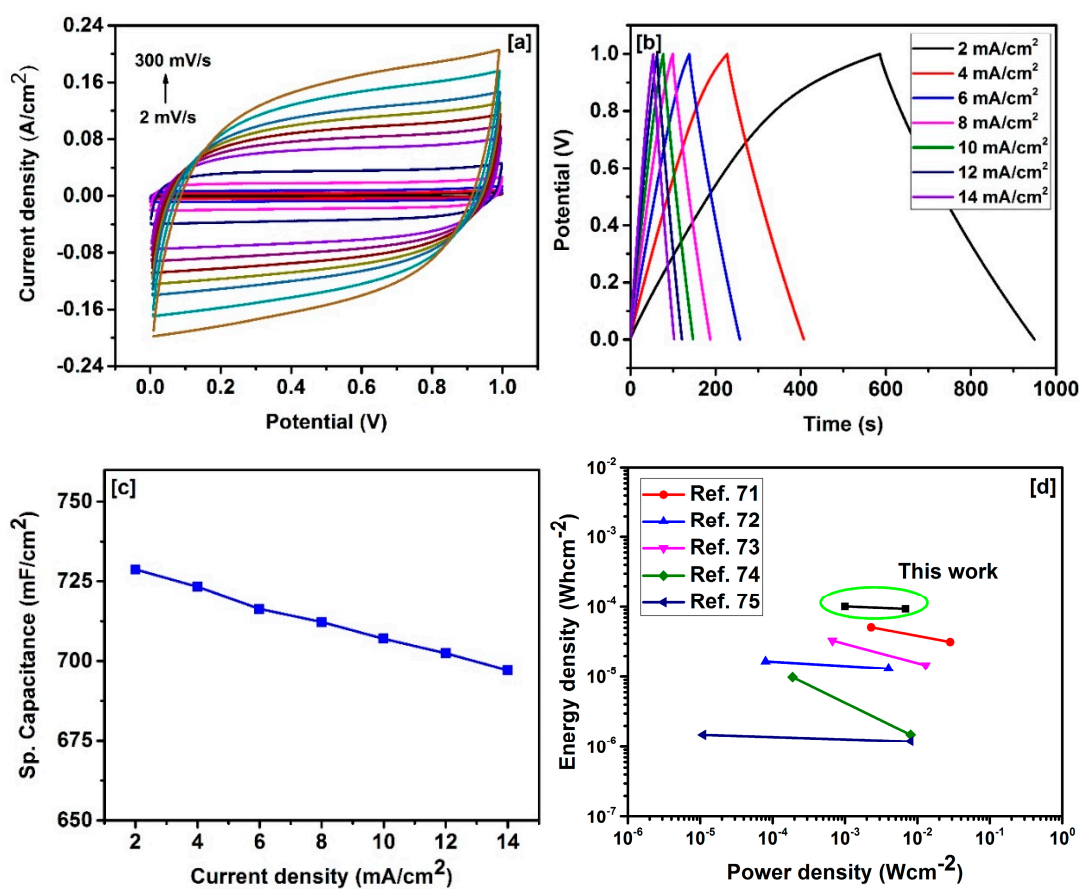


Figure 6. (a) CV curves at various scan rates; (b) GCD profiles at different current densities; (c) specific capacitances at different current densities of supercapacitor based on OPAC-1; and (d) Ragone plot comparing OPAC-1 to previous reports.

The temperature dependence of the OPAC-1 supercapacitor was studied by performing electrochemical measurements in the temperature range between 10 and 80 °C. Figure 7a displays the CV curves at 100 mV/s for various temperatures. Nearly rectangular CV curves were observed even for the higher temperatures, indicating retention of ideal EDL behavior and excellent stability in a broad temperature range. Figure 7b shows the GCD profiles of a supercapacitor at a current density of 10 mA/cm² for different temperatures. The discharge time continues to increase as the temperature increased from 10 to 80 °C. As a result, the charge storage capacity improved. We calculated the change in the capacitance at each temperature relative to capacitance at 10 °C (Figure 7c). A nearly 34% improvement in the capacitance was observed as the temperature increased from 10 to 80 °C at current densities of both 10 and 14 mA/cm².

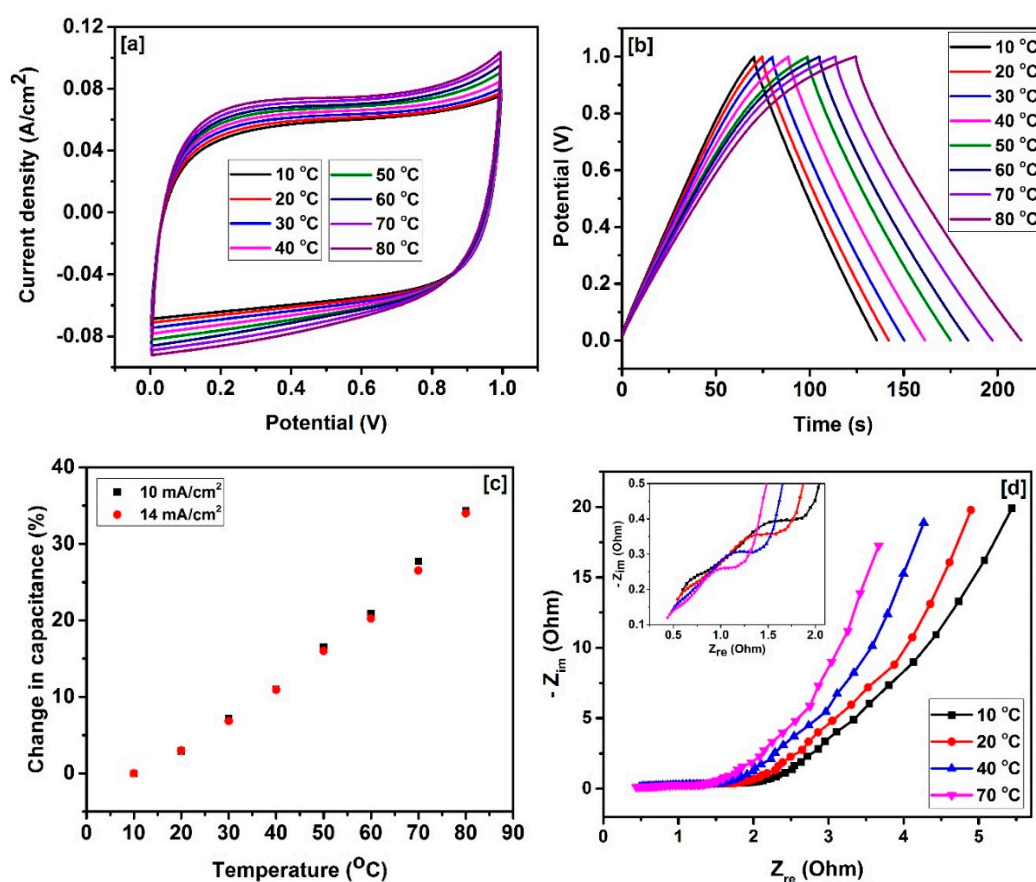


Figure 7. (a) CV curves for various temperatures at the scan rate of 100 mV/s; (b) GCD profiles for various temperatures at the current density of 10 mA/cm²; (c) % change of the specific capacitance against temperature and (d) Nyquist plots of selected temperatures with inset displaying magnification at higher frequency region for an OPAC-1 supercapacitor in 3 M KOH.

To investigate the temperature dependence of the charge storage process, we performed EIS measurements at different temperatures. Figure 7d compares the Nyquist plots of the OPAC-1 supercapacitor, measured at 10, 20, 40, and 70 °C. The features of the Nyquist plots, i.e., interception at Z_{real} axis in the high frequency region, diameter of the semi-circle at the middle–high frequency region, and length of the straight line at a low frequency range were associated with ohmic resistance of the solution, charge transfer resistance at the electrode–electrolyte interface, and ion diffusion resistance, respectively. All of these parameters decreased with an increase in temperature. The decrease in the series resistance was a result of the enhanced kinetic activity of electrolyte ions at elevated temperatures, rather than a change in the electrical properties of the electrode material [75]. The increased mobility

of electrolyte ions caused a 34% increment in the capacitance value with increasing temperature. Figure S7 shows the Bode impedance plots at 10, 20, 40, and 70 °C of the OPAC-1 device. It was noted that impedances below 1 Hz are almost equal for the considered temperatures, while for frequencies above 1 Hz, the impedance reduced faster with increasing temperature. These observations suggested that a supercapacitor based on pyrolyzed orange peel induced superior electrochemical performance at elevated temperatures.

3. Experimental

3.1. Preparation of Orange-Peel-Derived Porous Carbon

The waste orange peels were collected from households and subsequently washed, cleaned, and dried at 60 °C. Dried orange peels were crushed into a fine powder. The obtained orange peel powder was pre-carbonized at 400 °C for 2 h under a nitrogen atmosphere. Subsequently, chemical activation of the resultant carbon powder was performed using KOH as an activation agent. Carbon powder (1 g) and KOH pellets (1 g) were thoroughly mixed and pyrolyzed at 800 °C for 2 h inside a tube furnace under a nitrogen flow. The collected black mass was ground into powder and rinsed with 1 M HCl and DI water. The powder was dried at 60 °C for overnight. The obtained sample was named OPAC-1. Accordingly, porous carbons with a different activation level were prepared by changing the mass ratio of KOH (1:0.5, 1:2, 1:3); these samples were named OPAC-0.5, OPAC-2, and OPAC-3. The sample without KOH activation (OPUAC) was used as the control.

3.2. Structural Characterization

To investigate the crystallite structure of synthesized carbon, X-ray powder diffraction (Shimadzu X-ray diffractometer) was conducted using 2θ - θ scan, employing $\text{CuK}\alpha_1$ ($\lambda = 1.5406 \text{ \AA}$) as the radiation source. Raman spectroscopy (Model Innova 70, Coherent) was performed using an argon ion laser with a wavelength of 514.5 nm as the excitation source. Thermogravimetric analysis (TGA) was performed under nitrogen flow at a rate of 10 °C/min on a TA instrument (TA 2980). The morphology and microstructure of the carbon sample were determined by scanning electron microscopy (JEOL 7000 FE-SEM). Nitrogen adsorption/desorption isotherms were performed using an ASAP 2020 volumetric adsorption analyzer (Micrometrics, Norcross, GA, USA) at 77 K. Prior to the analysis, samples were degassed for 24 h at 90 °C. The Brunauer–Emmett–Teller (BET) method and Barrett–Joyner–Halenda (BJH) theory were used to calculate the specific surface area and derive pore size distributions, respectively.

3.3. Electrochemical Measurements

Electrochemical properties of the orange-peel-derived carbon (OPC) were evaluated utilizing a three-electrode system and a supercapacitor device. In both methods, electrodes were prepared by coating a viscous slurry of 80% (*w/w*) OPC, 10% (*w/w*) acetylene black, and 10% (*w/w*) polyvinylidene difluoride in N-methyl pyrrolidinone on to a nickel foam substrate. In a three-electrode system, electrochemical properties were studied using OPC-coated nickel foam as a working electrode, a platinum strip as a counter-electrode, and saturated calomel electrode as a reference electrode in three different electrolytes (3 M KOH, NaOH, and LiOH). A symmetrical supercapacitor was assembled by inserting an ion transporting layer between two identical OPAC-1 electrodes, followed by immersion in 3 M KOH electrolyte. The galvanostatic charge–discharge (GCD), cyclic voltammetry (CV), and electrochemical impedance spectroscopy (EIS) were completed using a VersaSTAT 4-500 electrochemical workstation (Princeton Applied Research, Oak Ridge, TN, USA). The frequency range of EIS varied from 0.05 Hz to 10 kHz with 10 mV of AC voltage amplitude. The gravimetric capacitance

(C_g/Fg^{-1}) for the three-electrode system and areal capacitance (C_a/Fcm^{-2}) for the supercapacitor were calculated from GCD measurements using the following equations:

$$C_g = \frac{I \times \Delta t}{\Delta V \times m} \quad (3)$$

$$C_a = \frac{I \times \Delta t}{\Delta V \times A} \quad (4)$$

where I is the discharge current (A), Δt is the discharge time (s), ΔV is the potential window (V), m is the mass (g) of the OPC, and A is the active area (cm^2) of the electrode. The energy density ($E/Whcm^{-2}$) and power density (P/Wcm^{-2}) of the symmetrical supercapacitor device were calculated according to the following equations:

$$E = \frac{C_a \times \Delta V^2}{7.2} \quad (5)$$

$$P = \frac{E \times 3600}{t} \quad (6)$$

where C_a is the areal capacitance (Fcm^{-2}) calculated from galvanostatic charge–discharge measurements, ΔV is the potential window (V), and t is the discharge time (s).

4. Conclusions

Sustainable and renewable carbon with a well-developed porous structure was synthesized via simple pyrolysis and chemical activation from readily available waste orange peels. A higher mass ratio of activation agent produced carbon with a larger surface area and a higher micropore fraction. However, it was found that carbon with mesopores and suitable pore size contribute to the higher capacitive performance. Among the studied alkaline electrolytes, these carbon materials exhibited optimum charge storage and rate capability in KOH electrolyte, along with 108% capacitance retention over 5000 cycles and identical electrochemical performance at different bending angles, indicating its potential as a stable and flexible electrode material. The prepared supercapacitor device showed superior energy density ($100.4 \mu Wh/cm^2$) and power density ($6.87 mW/cm^2$), improved temperature performance, and negligible IR drop, owing to the suitable pore size and higher degree of graphitization. This work presents the creation of proper electrode architecture and the selection of an efficient electrolyte system to enhance the charge storage capacity of biowaste-derived activated carbon for high-performance, sustainable, and cost-effective energy storage.

Supplementary Materials: Supplementary materials can be found at www.mdpi.com/1422-0067/3/3/25/s1.

Acknowledgments: Ram K. Gupta expresses his sincere acknowledgment to the Polymer Chemistry Initiative, Pittsburg State University for providing financial and research support.

Author Contributions: Ram K. Gupta conceived the project and designed the experiments. C. K. Ranaweera performed all the synthesis and performed some structural and electrochemical measurements. C. K. Ranaweera prepared the first draft of the manuscript. M. Ghimire and S. R. Mishra recorded the Scanning Electron Microscopic images and Raman spectra. All the authors reviewed and commented on the manuscript.

Conflicts of Interest: The authors declare no conflict of interest.

References

1. Beidaghi, M.; Gogotsi, Y.; Wang, Z.L.; Akyildiz, I.F.; Su, W.; Sankarasubramaniam, Y.; Cayirci, E.; Wang, Z.L.; Wu, W.; Wang, Z.L.; et al. Capacitive Energy Storage in Micro-Scale Devices: Recent Advances in Design and Fabrication of Micro-Supercapacitors. *Energy Environ. Sci.* **2014**, *7*, 867–884. [[CrossRef](#)]
2. Merlet, C.; Rotenberg, B.; Madden, P.A.; Taberna, P.-L.; Simon, P.; Gogotsi, Y.; Salanne, M. On the Molecular Origin of Supercapacitance in Nanoporous Carbon Electrodes. *Nat. Mater.* **2012**, *11*, 306–310. [[CrossRef](#)] [[PubMed](#)]

3. Choi, N.-S.; Chen, Z.; Freunberger, S.A.; Ji, X.; Sun, Y.-K.; Amine, K.; Yushin, G.; Nazar, L.F.; Cho, J.; Bruce, P.G. Challenges Facing Lithium Batteries and Electrical Double-Layer Capacitors. *Angew. Chem. Int. Ed.* **2012**, *51*, 9994–10024. [[CrossRef](#)] [[PubMed](#)]
4. Dyatkin, B.; Presser, V.; Heon, M.; Lukatskaya, M.R.; Beidaghi, M.; Gogotsi, Y. Development of a Green Supercapacitor Composed Entirely of Environmentally Friendly Materials. *ChemSusChem* **2013**, *6*, 2269–2280. [[CrossRef](#)] [[PubMed](#)]
5. Zhu, Y.; Murali, S.; Stoller, M.D.; Ganesh, K.J.; Cai, W.; Ferreira, P.J.; Pirkle, A.; Wallace, R.M.; Cychosz, K.A.; Thommes, M.; et al. Carbon-Based Supercapacitors Produced by Activation of Graphene. *Science* **2011**, *332*, 1537–1541. [[CrossRef](#)] [[PubMed](#)]
6. Niu, Z.; Zhou, W.; Chen, J.; Feng, G.; Li, H.; Ma, W.; Li, J.; Dong, H.; Ren, Y.; Zhao, D.; et al. Compact-Designed Supercapacitors Using Free-Standing Single-Walled Carbon Nanotube Films. *Energy Environ. Sci.* **2011**, *4*, 1440–1446. [[CrossRef](#)]
7. Xu, B.; Wu, F.; Chen, R.; Cao, G.; Chen, S.; Yang, Y. Mesoporous Activated Carbon Fiber as Electrode Material for High-Performance Electrochemical Double Layer Capacitors with Ionic Liquid Electrolyte. *J. Power Sources* **2010**, *195*, 2118–2124. [[CrossRef](#)]
8. Dai, Y.; Jiang, H.; Hu, Y.; Fu, Y.; Li, C. Controlled Synthesis of Ultrathin Hollow Mesoporous Carbon Nanospheres for Supercapacitor Applications. *Ind. Eng. Chem. Res.* **2014**, *53*, 3125–3130. [[CrossRef](#)]
9. Zequine, C.; Ranaweera, C.K.; Wang, Z.; Singh, S.; Tripathi, P.; Srivastava, O.N.; Gupta, B.K.; Ramasamy, K.; Kahol, P.K.; Dvornic, P.R.; et al. High performance and flexible supercapacitors based on carbonized bamboo fibers for wide temperature applications. *Sci. Rep.* **2016**, *6*, 31740. [[CrossRef](#)] [[PubMed](#)]
10. Qu, W.H.; Xu, Y.Y.; Lu, A.H.; Zhang, X.Q.; Li, W.C. Converting Biowaste Corn cob Residue into High Value Added Porous Carbon for Supercapacitor Electrodes. *Bioresour. Technol.* **2015**, *189*, 285–291. [[CrossRef](#)] [[PubMed](#)]
11. Wahid, M.; Puthusseri, D.; Phase, D.; Ogale, S. Enhanced capacitance retention in a supercapacitor made of carbon from sugarcane bagasse by hydrothermal pretreatment. *Energy Fuels* **2014**, *28*, 4233–4240. [[CrossRef](#)]
12. Peng, C.; Yan, X.B.; Wang, R.T.; Lang, J.W.; Ou, Y.J.; Xue, Q.J. Promising activated carbons derived from waste tea-leaves and their application in high performance supercapacitor electrodes. *Electrochim. Acta* **2013**, *87*, 401–408. [[CrossRef](#)]
13. Hou, J.; Cao, C.; Ma, X.; Idrees, F.; Xu, B.; Hao, X.; Lin, W. From rice bran to high energy density supercapacitors: A new route to control porous structure of 3D carbon. *Sci. Rep.* **2014**, *4*, 7260. [[CrossRef](#)] [[PubMed](#)]
14. Biswal, M.; Banerjee, A.; Deo, M.; Ogale, S.; Wang, G.; Zhang, L.; Zhang, J.; Frackowiak, E.; Béguin, F.; Dai, L.; et al. From dead leaves to high energy density supercapacitors. *Energy Environ. Sci.* **2013**, *6*, 1249–1259. [[CrossRef](#)]
15. Lv, Y.; Gan, L.; Liu, M.; Xiong, W.; Xu, Z.; Zhu, D.; Wright, D.S. A self-template synthesis of hierarchical porous carbon foams based on banana peel for supercapacitor electrodes. *J. Power Sources* **2012**, *209*, 152–157. [[CrossRef](#)]
16. Wu, F.-C.; Tseng, R.-L.; Hu, C.-C.; Wang, C.-C. Effects of pore structure and electrolyte on the capacitive characteristics of steam- and KOH-activated carbons for supercapacitors. *J. Power Sources* **2005**, *144*, 302–309. [[CrossRef](#)]
17. Valix, M.; Cheung, W.H.; McKay, G. Preparation of activated carbon using low temperature carbonisation and physical activation of high ash raw bagasse for acid dye adsorption. *Chemosphere* **2004**, *56*, 493–501. [[CrossRef](#)] [[PubMed](#)]
18. Guo, Y.; Zhang, H.; Tao, N.; Liu, Y.; Qi, J.; Wang, Z.; Xu, H. Adsorption of malachite green and iodine on rice husk-based porous carbon. *Mater. Chem. Phys.* **2003**, *82*, 107–115. [[CrossRef](#)]
19. Guo, Y.; Qi, J.; Jiang, Y.; Yang, S.; Wang, Z.; Xu, H. Performance of electrical double layer capacitors with porous carbons derived from rice husk. *Mater. Chem. Phys.* **2003**, *80*, 704–709. [[CrossRef](#)]
20. Girgis, B.S.; El-Hendawy, A.-N.A. Porosity development in activated carbons obtained from date pits under chemical activation with phosphoric acid. *Microporous Mesoporous Mater.* **2002**, *52*, 105–117. [[CrossRef](#)]
21. Caturla, F.; Molina-Sabio, M.; Rodríguez-Reinoso, F. Preparation of activated carbon by chemical activation with ZnCl₂. *Carbon N. Y.* **1991**, *29*, 999–1007. [[CrossRef](#)]
22. Wang, J.; Kaskel, S. KOH activation of carbon-based materials for energy storage. *J. Mater. Chem.* **2012**, *22*, 23710–23725. [[CrossRef](#)]

23. Maciá-Agulló, J.A.; Moore, B.C.; Cazorla-Amorós, D.; Linares-Solano, A. Activation of Coal Tar Pitch Carbon Fibres: Physical Activation vs. Chemical Activation. *Carbon N. Y.* **2004**, *42*, 1367–1370. [[CrossRef](#)]
24. Raymundo-Piñero, E.; Leroux, F.; Béguin, F. A High-Performance Carbon for Supercapacitors Obtained by Carbonization of a Seaweed Biopolymer. *Adv. Mater.* **2006**, *18*, 1877–1882. [[CrossRef](#)]
25. Ferrero, G.A.; Fuertes, A.B.; Sevilla, M.; Choi, N.-S.; Frackowiak, E.; Beguin, F.; Beguin, F.; Presser, V.; Balducci, A.; Frackowiak, E.; et al. From Soybean Residue to Advanced Supercapacitors. *Sci. Rep.* **2015**, *5*, 16618. [[CrossRef](#)] [[PubMed](#)]
26. Li, Y.; Wang, G.; Wei, T.; Fan, Z.; Yan, P. Nitrogen and Sulfur Co-Doped Porous Carbon Nanosheets Derived from Willow Catkin for Supercapacitors. *Nano Energy* **2016**, *19*, 165–175. [[CrossRef](#)]
27. Foreign Agricultural Service/USDA. *Citrus: World Markets and Trade*; USDA: Washington, DC, USA, 2017.
28. Grohmann, K.; Baldwin, E.A. Hydrolysis of Orange Peel with Pectinase and Cellulase Enzymes. *Biotechnol. Lett.* **1992**, *14*, 1169–1174. [[CrossRef](#)]
29. Marín, F.R.; Soler-Rivas, C.; Benavente-García, O.; Castillo, J.; Pérez-Alvarez, J.A. By-Products from Different Citrus Processes as a Source of Customized Functional Fibres. *Food Chem.* **2007**, *100*, 736–741. [[CrossRef](#)]
30. Widmer, W.; Zhou, W.; Grohmann, K. Pretreatment Effects on Orange Processing Waste for Making Ethanol by Simultaneous Saccharification and Fermentation. *Bioresour. Technol.* **2010**, *101*, 5242–5249. [[CrossRef](#)] [[PubMed](#)]
31. Prakash Maran, J.; Sivakumar, V.; Thirugnanasambandham, K.; Sridhar, R. Optimization of Microwave Assisted Extraction of Pectin from Orange Peel. *Carbohydr. Polym.* **2013**, *97*, 703–709. [[CrossRef](#)] [[PubMed](#)]
32. Feng, N.; Guo, X.; Liang, S.; Zhu, Y.; Liu, J. Biosorption of Heavy Metals from Aqueous Solutions by Chemically Modified Orange Peel. *J. Hazard. Mater.* **2011**, *185*, 49–54. [[CrossRef](#)] [[PubMed](#)]
33. Khaled, A.; El Nemr, A.; El-Sikaily, A.; Abdelwahab, O. Removal of Direct N Blue-106 from Artificial Textile Dye Effluent Using Activated Carbon from Orange Peel: Adsorption Isotherm and Kinetic Studies. *J. Hazard. Mater.* **2009**, *165*, 100–110. [[CrossRef](#)] [[PubMed](#)]
34. Martín, M.A.; Siles, J.A.; Chica, A.F.; Martín, A. Biomethanization of Orange Peel Waste. *Bioresour. Technol.* **2010**, *101*, 8993–8999. [[CrossRef](#)] [[PubMed](#)]
35. Ranaweera, C.K.; Ionescu, M.; Bilic, N.; Wan, X.; Kahol, P.K.; Gupta, R.K. Biobased Polyols Using Thiol-Ene Chemistry for Rigid Polyurethane Foams with Enhanced Flame-Retardant Properties. *J. Renew. Mater.* **2017**. [[CrossRef](#)]
36. Gao, Y.; Li, L.; Jin, Y.; Wang, Y.; Yuan, C.; Wei, Y.; Chen, G.; Ge, J.; Lu, H. Porous Carbon Made from Rice Husk as Electrode Material for Electrochemical Double Layer Capacitor. *Appl. Energy* **2015**, *153*, 41–47. [[CrossRef](#)]
37. Cheng, P.; Li, T.; Yu, H.; Zhi, L.; Liu, Z.; Lei, Z. Biomass-Derived Carbon Fiber Aerogel as a Binder-Free Electrode for High-Rate Supercapacitors. *J. Phys. Chem. C* **2016**, *120*, 2079–2086. [[CrossRef](#)]
38. Brebu, M.; Vasile, C. Thermal Degradation of Lignin—A Review. *Cellul. Chem. Technol.* **2010**, *44*, 353–363.
39. Paris, O.; Zollfrank, C.; Zickler, G.A. Decomposition and Carbonisation of Wood Biopolymers—A Microstructural Study of Softwood Pyrolysis. *Carbon N. Y.* **2005**, *43*, 53–66. [[CrossRef](#)]
40. Kastanaki, E.; Vamvuka, D.; Grammelis, P.; Kakaras, E. Thermogravimetric Studies of the Behavior of Lignite-biomass Blends during Devolatilization. *Fuel Process. Technol.* **2002**, *77*, 159–166. [[CrossRef](#)]
41. Mi, J.; Wang, X.; Fan, R.; Qu, W.; Li, W. Coconut-Shell-Based Porous Carbons with a Tunable Micro/Mesopore Ratio for High-Performance Supercapacitors. *Energy Fuels* **2012**, *26*, 5321–5329. [[CrossRef](#)]
42. Li, Y.; Li, Z.; Shen, P.K. Simultaneous Formation of Ultrahigh Surface Area and Three-Dimensional Hierarchical Porous Graphene-Like Networks for Fast and Highly Stable Supercapacitors. *Adv. Mater.* **2013**, *25*, 2474–2480. [[CrossRef](#)] [[PubMed](#)]
43. Wu, Z.-S.; Sun, Y.; Tan, Y.-Z.; Yang, S.; Feng, X.; Müllen, K. Three-Dimensional Graphene-Based Macro- and Mesoporous Frameworks for High-Performance Electrochemical Capacitive Energy Storage. *J. Am. Chem. Soc.* **2012**, *134*, 19532–19535. [[CrossRef](#)] [[PubMed](#)]
44. Ismanto, A.E.; Wang, S.; Soetaredjo, F.E.; Ismadi, S. Preparation of Capacitor's Electrode from Cassava Peel Waste. *Bioresour. Technol.* **2010**, *101*, 3534–3540. [[CrossRef](#)] [[PubMed](#)]
45. Cheng, P.; Gao, S.; Zang, P.; Yang, X.; Bai, Y.; Xu, H.; Liu, Z.; Lei, Z. Hierarchically Porous Carbon by Activation of Shiitake Mushroom for Capacitive Energy Storage. *Carbon N. Y.* **2015**, *93*, 315–324. [[CrossRef](#)]
46. Sing, K.S.W. Reporting Physisorption Data for Gas/solid Systems with Special Reference to the Determination of Surface Area and Porosity (Recommendations 1984). *Pure Appl. Chem.* **1985**, *57*, 603–619. [[CrossRef](#)]

47. Zhong, C.; Deng, Y.; Hu, W.; Qiao, J.; Zhang, L.; Zhang, J.; Burke, A.; Simon, P.; Gogotsi, Y.; Naoi, K.; et al. A Review of Electrolyte Materials and Compositions for Electrochemical Supercapacitors. *Chem. Soc. Rev.* **2015**, *44*, 7484–7539. [[CrossRef](#)] [[PubMed](#)]
48. Misnon, I.I.; Zain, N.K.M.; Aziz, R.A.; Vidyadharan, B.; Jose, R. Electrochemical Properties of Carbon from Oil Palm Kernel Shell for High Performance Supercapacitors. *Electrochim. Acta* **2015**, *174*, 78–86. [[CrossRef](#)]
49. Lee, J.H.; Park, N.; Kim, B.G.; Jung, D.S.; Im, K.; Hur, J.; Choi, J.W. Restacking-Inhibited 3D Reduced Graphene Oxide for High Performance Supercapacitor Electrodes. *ACS Nano* **2013**, *7*, 9366–9374. [[CrossRef](#)] [[PubMed](#)]
50. Xie, K.; Li, J.; Lai, Y.; Zhang, Z.; Liu, Y.; Zhang, G.; Huang, H. Polyaniline Nanowire Array Encapsulated in Titania Nanotubes as a Superior Electrode for Supercapacitors. *Nanoscale* **2011**, *3*, 2202–2207. [[CrossRef](#)] [[PubMed](#)]
51. Chang, J.; Gao, Z.; Wang, X.; Wu, D.; Xu, F.; Wang, X.; Guo, Y.; Jiang, K. Activated Porous Carbon Prepared from Paulownia Flower for High Performance Supercapacitor Electrodes. *Electrochim. Acta* **2015**, *157*, 290–298. [[CrossRef](#)]
52. Vadiyar, M.M.; Bhise, S.C.; Patil, S.K.; Kolekar, S.S.; Chang, J.-Y.; Ghule, A.V. Comparative Study of Individual and Mixed Aqueous Electrolytes with ZnFe₂O₄ Nano-Flakes Thin Film as an Electrode for Supercapacitor Application. *ChemistrySelect* **2016**, *1*, 959–966. [[CrossRef](#)]
53. Dubal, D.P.; Lee, S.H.; Kim, J.G.; Kim, W.B.; Lokhande, C.D. Porous Polypyrrole Clusters Prepared by Electropolymerization for a High Performance Supercapacitor. *J. Mater. Chem.* **2012**, *22*, 3044–3052. [[CrossRef](#)]
54. Qian, W.; Sun, F.; Xu, Y.; Qiu, L.; Liu, C.; Wang, S.; Yan, F. Human Hair-Derived Carbon Flakes for Electrochemical Supercapacitors. *Energy Environ. Sci.* **2013**, *7*, 379–386. [[CrossRef](#)]
55. Divyashree, A.; Hegde, G. Activated Carbon Nanospheres Derived from Bio-Waste Materials for Supercapacitor Applications—A Review. *RSC Adv.* **2015**, *5*, 88339–88352.
56. Bose, S.; Kuila, T.; Mishra, A.K.; Rajasekar, R.; Kim, N.H.; Lee, J.H. Carbon-Based Nanostructured Materials and Their Composites as Supercapacitor Electrodes. *J. Mater. Chem.* **2012**, *22*, 767–784. [[CrossRef](#)]
57. Salunkhe, R.R.; Lee, Y.-H.; Chang, K.-H.; Li, J.-M.; Simon, P.; Tang, J.; Torad, N.L.; Hu, C.-C.; Yamauchi, Y. Nanoarchitected Graphene-Based Supercapacitors for Next-Generation Energy-Storage Applications. *Chem. A Eur. J.* **2014**, *20*, 13838–13852. [[CrossRef](#)] [[PubMed](#)]
58. Obreja, V.V.N. On the Performance of Supercapacitors with Electrodes Based on Carbon Nanotubes and Carbon Activated material—A Review. *Phys. E Low-dimens. Syst. Nanostruct.* **2008**, *40*, 2596–2605. [[CrossRef](#)]
59. Guo, Y.; Shi, Z.; Chen, M.; Wang, C. Hierarchical Porous Carbon Derived from Sulfonated Pitch for Electrical Double Layer Capacitors. *J. Power Sources* **2014**, *252*, 235–243. [[CrossRef](#)]
60. Du, S.; Wang, L.; Fu, X.; Chen, M.; Wang, C. Hierarchical Porous Carbon Microspheres Derived from Porous Starch for Use in High-Rate Electrochemical Double-Layer Capacitors. *Bioresour. Technol.* **2013**, *139*, 406–409. [[CrossRef](#)] [[PubMed](#)]
61. Wang, R.; Wang, P.; Yan, X.; Lang, J.; Peng, C.; Xue, Q. Promising Porous Carbon Derived from Celtuce Leaves with Outstanding Supercapacitance and CO₂ Capture Performance. *ACS Appl. Mater. Interfaces* **2012**, *4*, 5800–5806. [[CrossRef](#)] [[PubMed](#)]
62. Hegde, G.; Abdul Manaf, S.A.; Kumar, A.; Ali, G.A.M.; Chong, K.F.; Ngaini, Z.; Sharma, K.V. Biowaste Sago Bark Based Catalyst Free Carbon Nanospheres: Waste to Wealth Approach. *ACS Sustain. Chem. Eng.* **2015**, *3*, 2247–2253. [[CrossRef](#)]
63. Xie, Q.; Bao, R.; Zheng, A.; Zhang, Y.; Wu, S.; Xie, C.; Zhao, P. Sustainable Low-Cost Green Electrodes with High Volumetric Capacitance for Aqueous Symmetric Supercapacitors with High Energy Density. *ACS Sustain. Chem. Eng.* **2016**, *4*, 1422–1430. [[CrossRef](#)]
64. Yang, C.-S.; Jang, Y.S.; Jeong, H.K. Bamboo-Based Activated Carbon for Supercapacitor Applications. *Curr. Appl. Phys.* **2014**, *14*, 1616–1620. [[CrossRef](#)]
65. Teo, E.Y.L.; Muniandy, L.; Ng, E.-P.; Adam, F.; Mohamed, A.R.; Jose, R.; Chong, K.F. High Surface Area Activated Carbon from Rice Husk as a High Performance Supercapacitor Electrode. *Electrochim. Acta* **2016**, *192*, 110–119. [[CrossRef](#)]
66. Du, X.; Zhao, W.; Wang, Y.; Wang, C.; Chen, M.; Qi, T.; Hua, C.; Ma, M. Preparation of Activated Carbon Hollow Fibers from Ramie at Low Temperature for Electric Double-Layer Capacitor Applications. *Bioresour. Technol.* **2013**, *149*, 31–37. [[CrossRef](#)] [[PubMed](#)]

67. Zhang, J.; Gong, L.; Sun, K.; Jiang, J.; Zhang, X. Preparation of Activated Carbon from Waste Camellia Oleifera Shell for Supercapacitor Application. *J. Solid State Electrochem.* **2012**, *16*, 2179–2186. [[CrossRef](#)]
68. Yang, Y.; Ruan, G.; Xiang, C.; Wang, G.; Tour, J.M. Flexible Three-Dimensional Nanoporous Metal-Based Energy Devices. *J. Am. Chem. Soc.* **2014**, *136*, 6187–6190. [[CrossRef](#)] [[PubMed](#)]
69. Cui, H.; Zhu, G.; Liu, X.; Liu, F.; Xie, Y.; Yang, C.; Lin, T.; Gu, H.; Huang, F. Niobium Nitride Nb₄N₅ as a New High-Performance Electrode Material for Supercapacitors. *Adv. Sci.* **2015**, *2*, 1500126. [[CrossRef](#)] [[PubMed](#)]
70. Yu, J.; Lu, W.; Pei, S.; Gong, K.; Wang, L.; Meng, L.; Huang, Y.; Smith, J.P.; Booksh, K.S.; Li, Q.; et al. Omnidirectionally Stretchable High-Performance Supercapacitor Based on Isotropic Buckled Carbon Nanotube Films. *ACS Nano* **2016**, *10*, 5204–5211. [[CrossRef](#)] [[PubMed](#)]
71. Cao, J.; Wang, Y.; Chen, J.; Li, X.; Walsh, F.C.; Ouyang, J.-H.; Jia, D.; Zhou, Y. Three-Dimensional Graphene Oxide/polypyrrole Composite Electrodes Fabricated by One-Step Electrodeposition for High Performance Supercapacitors. *J. Mater. Chem. A* **2015**, *3*, 14445–14457. [[CrossRef](#)]
72. Liu, N.; Ma, W.; Tao, J.; Zhang, X.; Su, J.; Li, L.; Yang, C.; Gao, Y.; Golberg, D.; Bando, Y. Cable-Type Supercapacitors of Three-Dimensional Cotton Thread Based Multi-Grade Nanostructures for Wearable Energy Storage. *Adv. Mater.* **2013**, *25*, 4925–4931. [[CrossRef](#)] [[PubMed](#)]
73. Le, V.T.; Kim, H.; Ghosh, A.; Kim, J.; Chang, J.; Vu, Q.A.; Pham, D.T.; Lee, J.-H.; Kim, S.-W.; Lee, Y.H. Coaxial Fiber Supercapacitor Using All-Carbon Material Electrodes. *ACS Nano* **2013**, *7*, 5940–5947. [[CrossRef](#)] [[PubMed](#)]
74. Weng, Z.; Su, Y.; Wang, D.-W.; Li, F.; Du, J.; Cheng, H.-M. Graphene-Cellulose Paper Flexible Supercapacitors. *Adv. Energy Mater.* **2011**, *1*, 917–922. [[CrossRef](#)]
75. Masarapu, C.; Zeng, H.F.; Hung, K.H.; Wei, B. Effect of Temperature on the Capacitance of Carbon Nanotube Supercapacitors. *ACS Nano* **2009**, *3*, 2199–2206. [[CrossRef](#)] [[PubMed](#)]



© 2017 by the authors. Licensee MDPI, Basel, Switzerland. This article is an open access article distributed under the terms and conditions of the Creative Commons Attribution (CC BY) license (<http://creativecommons.org/licenses/by/4.0/>).